Long-Range Electron Transfer over Graphene-Based Catalyst for High-Performing Oxygen Reduction Reactions: Importance of Size, N-doping, and Metallic Impurities

Chang Hyuck Choi,[†,§] Hyung-Kyu Lim,[‡,§] Min Wook Chung,[‡] Jong Cheol Park,[†,∥] Hyeyoung Shin,[‡] Hyungjun Kim,*[‡] and Seong Ihl Woo*[†,‡]

[†]Department of Chemical and Biomolecular Engineering and [‡]Graduate School of EEWS, Korea Advanced Institute of Science and Technology, Daejeon 305-701, Republic of Korea

[∥]Connect and Development Team 1, GS Caltex, Deajeon 305-380, Republic of Korea

S *Supporting Information*

ABSTRACT: N-doped carbon materials are considered as next-generation oxygen reduction reaction (ORR) catalysts for fuel cells due to their prolonged stability and low cost. However, the underlying mechanism of these catalysts has been only insufficiently identified, preventing the rational design of high-performing catalysts. Here, we show that the first electron is transferred into O_2 molecules at the outer Helmholtz plane (ET-OHP) over a long range. This is in sharp contrast to the conventional belief that O_2 adsorption must precede the ET step and thus that the active site must possess as good an O_2 binding character as that which occurs on metallic catalysts. Based on the ET-OHP mechanism, the location of the electrode potential dominantly characterizes the ORR activity. Accordingly, we demonstrate that the electrode potential can be elevated by reducing the graphene size and/or including metal impurities, thereby enhancing the ORR activity, which can be transferred into single-cell operations with superior stability.
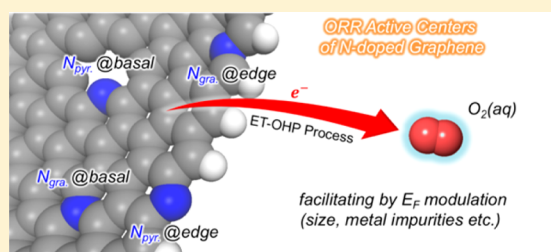
1. INTRODUCTION

Polymer electrolyte membrane fuel cells (PEMFCs) have advanced substantially over the past few decades, both in fundamental and in engineering aspects.[1] However, significant breakthroughs are still needed to lower their cost and enhance their durability in order to eventually replace conventional combustion engines in next-generation applications and replace fossil fuels with clean hydrogen fuels. The most serious problem of current PEMFC technology is its prohibitively expensive cost per unit of power output; this high cost is the result of the electrodes, which contain a large amount of expensive Pt and have limited long-term stability. To resolve these problems, various types of transition-metal-based catalysts have been proposed, such as chalcogenides (e.g., RuSe and CoSe) and oxycarbonitrides (e.g., TaOCN).[2] However, these types of catalysts are easily corroded in the severe acidic environment around the electrode. As stated by Jasinski[3] and Yeager,[4] carbon-based materials can be considered promising alternatives to Pt due to their cost-effectiveness and high stability.[2]

For a rational design that will maximize the oxygen reduction reaction (ORR) performance, it is critical to understand the underlying ORR mechanism of N-doped carbon catalysts. Despite the numerous experimental and theoretical studies that have been performed, many controversies remain regarding the ORR mechanism, particularly about the nature of the catalytic active sites; it has been suggested that N-doped carbon serves

as an active center,[5−7] while it has also been suggested that the nitrogen-coordinated metal ($Me-N_x$) complex serves as an active center.[8−11] This confusion is mostly due to the complexity of the systems; the nature of the active center will presumably be found to be dependent on the catalyst preparation methods (e.g., choice of precursors and heat-treatment temperature) and on the operation conditions.

Regarding the N-doped carbon active centers, there have been many debates about their spatial location, which is thought to be either at the edge or at the basal plane of the graphene; there is also debate about the chemical nature of these centers, as to whether they have either pyridinic-N sites[12,13] or graphitic-N sites.[14,15] Because it has a lone pair of electrons, which enhances O_2 adsorption,[13,16] pyridinic-N has often been regarded as the catalytic active site. However, recent experiments using chemical vapor deposition (CVD)-grown graphene or carbon black have demonstrated the prominent role of graphitic-N sites in ORR.[17,18] Moreover, for samples prepared using reduced graphene oxides, Lai et al. suggested that the limiting ORR current of graphene-based catalysts in alkaline media is determined by graphitic-N.[19] However, a mechanistic understanding of the graphitic-N catalyzing process is still elusive, especially in acidic conditions, because quantum mechanical theory predicts that oxygen binding near graphitic-

N sites is not favored unless a nitrogen atom is specifically located immediately at the edge site.[20]

In this study we investigated the ORR mechanism of a graphene-based catalyst and tried to resolve the highly questionable roles of N-doping and metallic phase through extensive characterization methods, including transmission electron microscopy (TEM), Mössbauer spectroscopy, elemental analyses (EA) with inductively coupled plasma (ICP), X-ray photoelectron spectroscopy (XPS), ultraviolet photoelectron spectroscopy (UPS), Raman spectroscopy, and Brunauer–Emmett–Teller (BET) surface analysis. We also used various poisoning experiments coupled with quantum mechanical density functional theory (DFT) calculations. Toward a practical usage of graphene-based catalysts in the future, we examined the ORR activity within acidic media; ORR activity was maximized to yield mostly a four-electron reaction pathway, which can be realized using nanosized N-doped graphene that has been fragmentized via a simple ball-milling process that is advantageous in enabling large scale production.

2. EXPERIMENTAL SECTION

2.1. Materials Synthesis. Graphite oxide (GO) was prepared by chemical oxidation of graphite. Depending on whether or not the ball-milling process was performed, the prepared samples were named bNGr and NGr, respectively, after surface modifications via pyrolysis with dicyandiamide in the presence of metal chlorides and subsequent acid treatment (Scheme 1).

Scheme 1. Schematic Diagram of the Catalyst Preparations[a]

P1: Chemical exfoliation
P2: Ball-milling
P3: Surface modification
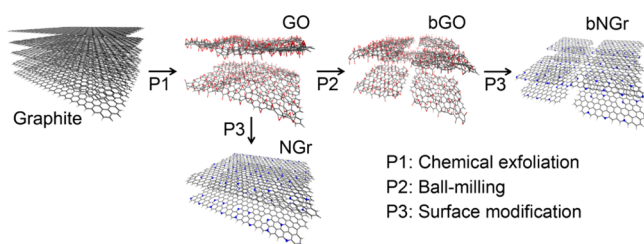
[a]black, carbon; red, oxygen; and blue, nitrogen atoms.

In detail, graphite (3 g) was dispersed in a mixture of concentrated sulfuric acid (H_2SO_4, 360 mL) and phosphoric acid (H_3PO_4, 40 mL). Potassium permanganate (18 g) was added, and the solution was reacted at 50 °C for 12 h. After cooling to room temperature, the solution was poured onto ice (400 mL) with hydrogen peroxide (35% H_2O_2, 5 mL) and was stirred for 1 h. A yellow powder was obtained by centrifugation at 6000 rpm for 30 min and sonicated in hydrochloric acid (5 M HCl, 200 mL) for 10 min. The GO was obtained after centrifugation with water and drying in a vacuum oven (70 °C). Fragmentation of GO (bGO) was performed using a ball-milling process. In order to prohibit Fe contamination, ball-milling was performed for 12 h at 300 rpm rotation speed with zirconium balls (5 mm in diameter) in a Nalgene bottle (250 mL capacity) containing water (100 mL). The bNGr was synthesized by surface modification of bGO. The bGO (0.5 g) was dispersed in an aqueous solution (100 mL) of dicyandiamide ($C_2H_4N_4$, 0.5 g), cobalt chloride ($CoCl_2 \cdot 6H_2O$, 22 mmol), and iron chloride ($FeCl_2 \cdot 4H_2O$, 66 mmol). The amount of metals (Co and Fe) was set at 1 wt % relative to the weight of GO. After sonication for 1 h, the solvent was evaporated at 80 °C under 300 mbar. The obtained mixture was further dried in a vacuum oven (70 °C) and then pyrolyzed at 900 °C under Ar protection (50 mL min^{-1}) for 3 h. Any acid unstable phases were dissolved in sulfuric acid (0.5M, 100 mL) at 80 °C for 8 h. The bNGr was gathered by filtration, washing with water, and drying in a vacuum oven (70 °C); it was then

heat-treated again at 900 °C under Ar protection (50 mL min^{-1}) for 3 h. The NGr was prepared using the same method as was used for the bNGr, except for the ball-milling process. As a model catalyst for poisoning experiments, pyrolyzed iron(II) phthalocyanine on activated carbon (FePc/C) was synthesized by heat-treatment of FePc on Ketjen black EC-300J (Fe content = 1 wt %) at 800 °C under an NH_3 flow (150 mL min^{-1}) for 2 h, acid treatment (same procedure as that used for bNGr), and then secondary heat treatment (800 °C under 150 mL min^{-1} of NH_3 flow for 2 h).

2.2. Electrochemical Characterizations. Half-cell experiments were performed using a CHI700D (CH Instruments Inc.) and a RRDE-3A (ALS Co.) in a three-electrode beaker cell equipped with a Pt wire counter electrode (002233, ALS Co.), an Ag/AgCl reference electrode (012167, ALS Co.; calibrated and converted to RHE scale), and a ring disk electrode (011169, ALS Co.). The graphene-derived catalysts (10 mg) were dispersed in a Nafion ink solution (1 mL, 1 wt % Nafion content), and then ink (5 μL) was dropped onto the glassy carbon (3 mm) of the ring disk electrode. The catalyst loading in the working electrode was 714 μg cm^{-2}. Linear sweep voltammetry (LSV) was performed in a 0.1 M $HClO_4$ electrolyte bubbled by nitrogen or oxygen with a 5 mV s^{-1} scan rate from 1.04 to 0.14 V (vs RHE) and 900 rpm rotation speed. The ORR currents were derived by subtracting the LSV results for the nitrogen-purged electrolyte from those of the oxygen-purged electrolyte, in order to remove the capacitance of the catalysts. For comparison, Pt/C (E-tek, 20 wt %) was also examined, and the loading of Pt on the working electrode was 20 μg$_{Pt}$ cm^{-2}. A Tafel-plot based on kinetic current in the ORRs was obtained using the following equation.

$$\frac{1}{I} = \frac{1}{I_k} + \frac{1}{I_d} \tag{1}$$

where I is the current from the LSV results, I_k is the kinetic current, and I_d is the diffusion current. The mass activities and specific activities were calculated through normalization of the kinetic current at 0.75 V (vs RHE) using the mass and the surface area (obtained from BET analyses) of the catalysts. The H_2O_2 formation yields were derived from the current at the Pt ring disk electrode of the rotating ring disc electrode (RRDE), applied to a constant potential of 1.2 V (vs RHE); the following equations were used.

$$H_2O_2(\%) = 200 \times \frac{I_R/N}{I_R/N + I_D} \tag{2}$$

$$n = 4 \times \frac{I_D}{I_R/N + I_D} \tag{3}$$

where I_R is the ring current, I_D is the disk current, N is the collection efficiency (0.42; calibrated by a $[Fe(CN)_6]^{4-}/[Fe(CN)_6]^{3-}$ system and very similar to the value of 0.422 provided by the manufacturer), and n is the number of electrons transferred in ORR. Methanol tolerance was examined at a constant potential of 0.6 V (vs RHE) in O_2-bubbled 0.1 M $HClO_4$, and methanol (1 mL) was injected after 1 min. Square wave voltammetry (SWV) results were obtained in nitrogen-purged 0.1 M $HClO_4$ with a 2 mV potential increment, 5 mV potential amplitude, and 5 Hz frequency. The KCN poisoning was measured in the same conditions as those used in the LSV experiment, with the addition of the KCN (10 mM). CO and H_2S poisonings were conducted using current−time chronoamperometry at 0.4 V (vs RHE) under bubbling of a mixture gas (O_2:poison gas = 1:1, v:v) in a 0.1 M $HClO_4$ electrolyte. Potential of zero charge was examined in 2 mM of NaF electrolyte with a 100 mHz frequency and a 10 mV potential amplitude. The equivalent series resistance was obtained in a capacitor-type cell that was fabricated with a glass filter paper, two symmetric electrodes (1 mg of an active material), and 0.1 M $HClO_4$ electrolyte.

The membrane electrode assembly (active area = 5 cm^2) was fabricated for PEMFC operation with Nafion (NR212, Du Pont) as a membrane, Pt-loaded carbon cloth (1 mg$_{Pt}$ cm^{-2}, E117CN, Fuel Cell Earth) as an anode electrode, and a bNGr-sprayed gas diffusion layer as a cathode electrode. The cathode electrode was prepared by
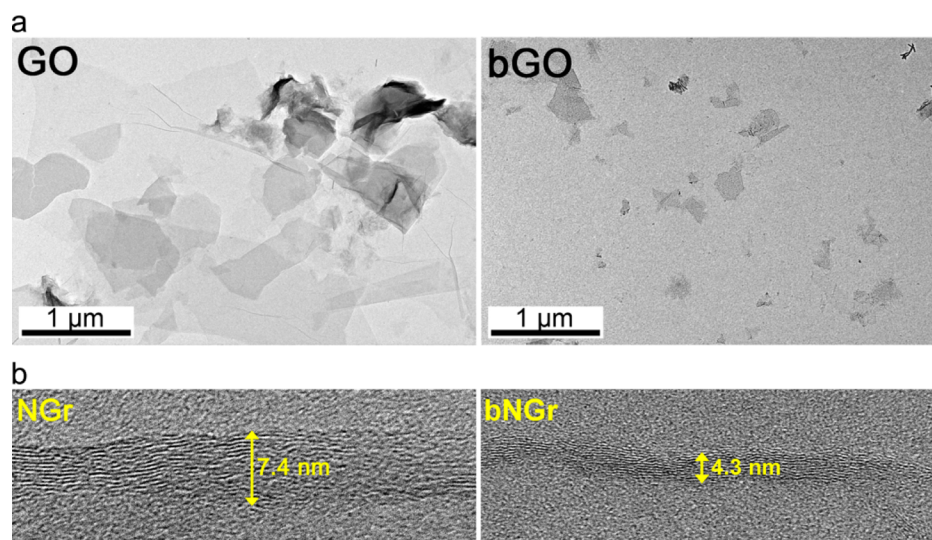
Figure 1. (a) TEM images of GO and bGO. (b) Thicknesses of the NGr and bNGr catalysts obtained from HRTEM images.

spraying bNGr ink (bNGr:Nafion = 1:1.5) on the gas diffusion layer (GDL 10 BC, SGL group) and the loading of bNGr was 3.9 mg cm². The assembly was pressed at 125 °C for 150 s under 80 kgf cm⁻² of pressure. Single cell performance was examined using an 890CL (Scribner Associates Inc.) at 80 °C operation temperature. The hydrogen and oxygen gases were flowed (5.5 L min⁻¹) into the PEMFCs with 2 bar of back pressure, and the system was humidified at 90 °C. A stability test was performed at 0.4 V over 1100 h, and the cell was dried for 50 h under standard conditions (room temperature and atmospheric pressure) after 500 h of operation.

2.3. Physical Characterizations. The physical properties of the graphene-derived catalysts were characterized by TEM, Mössbauer spectroscopy, EA, ICP, XPS, UPS, Raman spectroscopy, and BET surface analyses. The TEM images were taken using a JEM2100-F (Jeol Ltd.) operated at 200 kV. Mössbauer spectroscopy (electromechanical type, MR-531) was performed with a constant acceleration at room temperature using ^{57}Co (50 mCi) in an Rh matrix as the γ-ray source; device was calibrated using α-Fe foil. The compositions of the prepared catalysts were obtained with element analyses performed using a FlashEA 1112 and from ICP analyses performed using a POLY SCAN 61 E (Hewlett-Packard). The XPS and UPS analyses were performed using a Sigma Probe (Thermo VG Scientific) equipped with a microfocused monochromator X-ray source and an He I UV source. XPS-N$_{1s}$ peaks were deconvoluted by pyridinic- (398.6 eV), graphitic-, or pyrrolic-N (401 ± 0.5 eV) and pyridinic-oxide (403 eV). Raman spectroscopy was performed using a LabRAM HR UV/vis/NIR (Horiba Jobin Yvon) with a laser source of 514 nm. The BET surface area analyses were performed on a Micrometrics ASAP 2010 apparatus at 77 K.

2.4. DFT Calculations. DFT calculations were conducted using the exchange-correlation functional of Perdew–Burke–Ernzerhof (PBE).[21] Jaguar 7.9, along with the Pople 6-31G* basis set, was used to calculate the Fermi level for the series of graphene dots.[22] The ground-state geometries were fully optimized for negative, neutral, and positive charged states to evaluate the reasonable ionization potential (IP) and electron affinity (EA). The Fermi level was calculated using the formula, −(IP + EA)/2. Fermi level calculations for 3D periodic models (2D model on *x*–*y* plane with a 15 Å vacuum slab along the *z*-axis), such as 5 × 5 infinite and arm-chair-edged nanoribbon graphenes, used the Vienna Ab initio Simulation Package (VASP).[23] The electron–ion interaction was considered in the form of the projector-augmented wave (PAW) method, with a plane wave up to energy of 600 eV. The ground-state geometries were fully optimized, and then the precise density of the states was calculated with the tetrahedron method, including Blöchl corrections. The *k*-points were generated by 5 × 5 × 1 for infinite models and 1 × 7 × 1 for nanoribbon models using the Monkhorst–Pack scheme. The Fermi

level was modified by referencing the energy level of the vacuum for these models. Searches for O$_2$ and ●OOH adsorption sites on various N-doped sites were also conducted using the VASP program with 500 eV plane wave cut off energy. Gamma centered 5 × 5 × 1 *k*-points were used for bulk models and Monkhrost-Pack 4 × 1 × 1 *k*-points were used for edge models. After fully optimizing the adsorbed structures, frequency calculations were conducted to calculate the vibrational internal energy and entropy, based on a partial Hessian consisted with atoms of adsorbate molecules and adjacent carbon. Vibrational temperatures under 300 K were disregarded. To estimate the enthalpy changes during the solvation process, the Poisson–Boltzmann (PB) implicit solvation model, implemented in the VASP program,[24] was employed using a dielectric constant $\varepsilon = 80$ for water (we neglect the cavitation energy contribution). To calculate the appropriate free energy terms in the solvation state, we also assumed that the total quantities of energy and entropy for the translational and the rotational motion in the gas phase were fully quenched in the solvated state, which means that only vibrational motions are effective in the solvated state. The formulas for calculating adsorption energy and adsorption free energy in solvation state are as follows.

For adsorption energy ΔE_{ads}, eq 4:

$$\Delta E_{ads} = E_{adsorbate\text{-}surface} - E_{surface} - E_{adsorbate} \qquad (4)$$

where each energy component (E) comes from DFT electronic self-consistent energy in the gas phase.

For adsorption free energy in the solvation state ($\Delta G_{ads}(aq)$, eq 5):

$$\Delta G_{ads}(aq) = G_{adsorbate\text{-}surface}(aq) - G_{surface}(aq) - G_{adsorbate}(aq) \qquad (5)$$

3. RESULTS AND DISCUSSION

GO has several micrometers (1−5 μm) of sheet-like morphology (Figure 1a); the ball-milling process effectively reduces the size of the GO sheets to several hundreds of nanometers (50−500 nm). Without ball-milling, NGr exhibits a highly restacked and aggregated morphology (Figures 1b and S1), while bNGr shows a much lower thickness (nearly 4 nm) and maintains a graphene-like morphology. This morphology of bNGr can be attributed to the relatively small size of the flakes, which weakens the van der Waals forces,[25] and to the ball-milling process, which mechanically helps prevent restacking,[26] resulting in an increased surface area of few-layer graphenes from 90.1 m² g⁻¹ for NGr to 141.3 m² g⁻¹ for bNGr.

From the electrochemical measurements, bNGr can be seen to show significantly improved ORR activity compared to that of NGr. Using LSV, performed in a 0.1 M HClO$_4$ electrolyte (Figure 2a), we calculated the kinetic current toward the ORRs
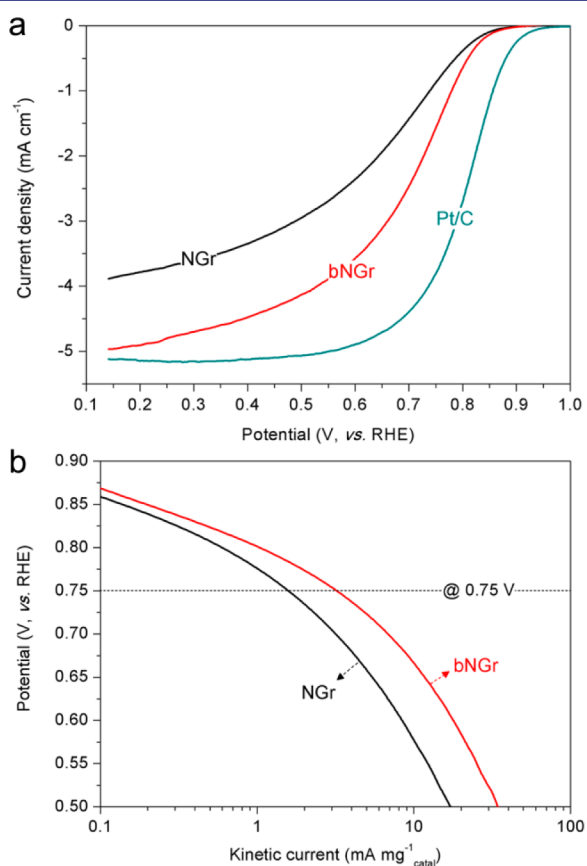

Figure 2. ORR responses of the graphene-based catalysts. (a) Capacitance-eliminated LSV results for the prepared catalysts (catalyst loading =714 μg cm^{-2}) with a 5 mV s^{-1} scan rate and 900 rpm electrode rotation speed under O$_2$ bubbling in a 0.1 M HClO$_4$ electrolyte. The result for Pt/C (Pt-loading = 20 μg cm^{-2}) is added for comparison. (b) Tafel-plots derived from LSV results for the prepared catalysts.

according to the mass activity values; the bNGr catalyst demonstrates an enhanced ORR mass activity of 3.4 mA mg^{-1}$_\text{catal}$, while the NGr catalyst shows a mass activity of 1.6 mA mg^{-1}$_\text{catal}$ at 0.75 V (Figure 2b). The specific activity, normalized using the surface area of the prepared graphene-materials, is also noticeably improved after the ball-milling process (24.0 mA m^{-2} for bNGr but 17.5 mA m^{-2} for NGr at 0.75 V). This indicates that the enhanced mass activity cannot be fully attributed to the change of the surface area and that either the turnover frequency (TOF) or the surface density of the active sites of bNGr is higher than that of NGr. In Figure 3, chronoamperometric results obtained at 0.6 V further support that ORR is enhanced after the ball-milling process (ORR currents: bNGr > NGr); these results also showed that this material has an excellent tolerance against methanol oxidation reactions.

To investigate the ORR pathway, H$_2$O$_2$ production yields and the number of transferred electrons were determined using RRDE at 900 rpm rotating speed (Figure 4). The ball-milling process suppresses the 2e$^-$ pathway in ORRs, and the H$_2$O$_2$
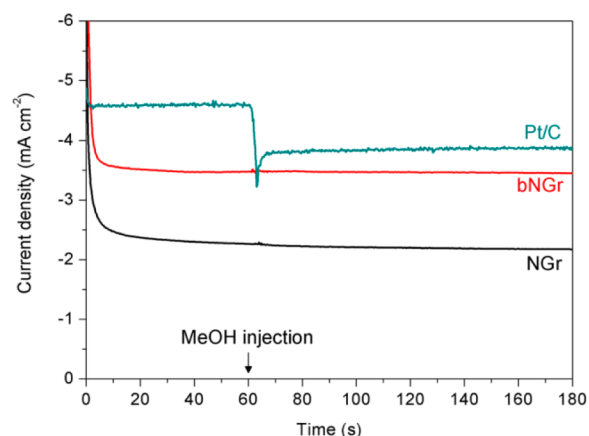

Figure 3. Methanol-tolerance experiments conducted at 0.6 V (vs RHE) under O$_2$ bubbling. Methanol is injected in the electrolyte at 1 min.
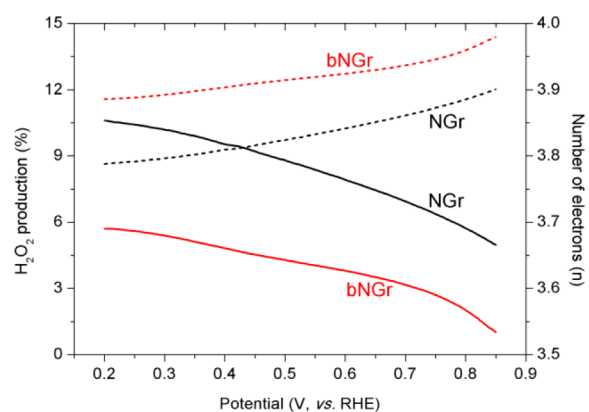
Figure 4. Calculated H$_2$O$_2$ production yields (solid line) and number of electrons transferred (dotted line) from rotating Pt-ring disk electrode (RRDE) when 1.2 V (vs RHE) applied to the Pt ring.

yield for bNGr is <6% for the entire potential range, indicating a dominant 4e$^-$ pathway in our samples. In the 4e$^-$ pathway of the ORRs, the initial electron-transfer (ET) step from the electrode to the O$_2$ molecules is known to be the rate-determining step.[27] The Tafel slope of -68 mV dec^{-1} (Figure 2b) also reveals that the first ET is the rate-determining step under Temkin conditions of intermediate adsorption.[28]

3.1. Possible Candidates for Catalytic Active Sites in bNGr. There exist three possible candidates for catalytic active sites in bNGr: Me-N$_x$ sites, N-doped carbons at the edge of the graphene, and N-doped carbons at the basal plane of the graphene. From EA-ICP (Table S1), it was found that bNGr contains 1.7 wt % of Fe and 0.3 wt % of Co even after acid treatment steps. Under the extreme assumption that all of these metal atoms are exposed on the catalyst surface as single atoms and that they are solely responsible for the observed ORR activity, TOF is estimated to be 10^{-1} ~ 10^{-2} s^{-1}, which range is unreasonably higher than the that of the TOF of Pt (10^{-2} ~ 10^{-3} s^{-1}).[29] Similarly, if we carry out an order-estimation of the number of N-doped sites located at the edges of graphene sheets of various sizes (ranging in diameter from 0.2 to 2 μm; see TEM images in Figure S1) and normalize the observed activity with these numbers, the estimated TOF is unrealistically high, in the range of 10^{1} ~ 10^{-1} s^{-1} (Figure S2). Therefore, at least in our bNGr sample, in which most metals are considered to be inaccessible to O$_2$, we need to take the
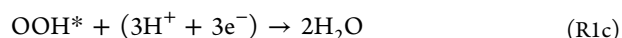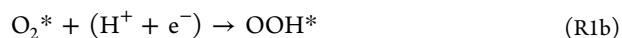
Scheme 2. Starting from the Solvated O_2 Molecules, Pathway Is Divided into ET-OHP and ET-IHP Processes[a]

* for edge graphitic N-doped site
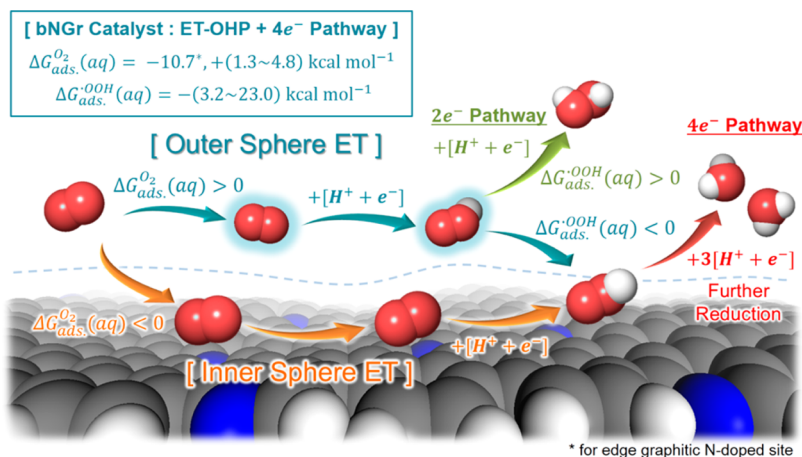
[a]For ET-OHP, O_2 adsorption is not necessary ($\Delta G_{ads}^{O_2} > 0$), and the rate of ET is strongly affected by the ionic strength of electrolyte; for ET-IHP, it is important to find good O_2 adsorption sites ($\Delta G_{ads}^{O_2} < 0$), and the electron can be injected into the O_2 π^* orbital through orbital−orbital interaction at a femtosecond time scale. From the DFT energetics, only the graphitic-N sites at the edge of the graphene can adsorb O_2 and enable the ET-IHP mechanism only at these sites; however, this mechanism cannot be fully attributed to the observed ORR kinetics. On the basal plane where O_2 adsorption is unfavored, therefore, the ET-OHP process will dominantly occur. After the formation of ●OOH at the end of the ET-OHP process, ●OOH immediately adsorbs onto the N-doped graphene surface ($\Delta G_{ads}^{●OOH} < 0$); this allows further stable reductions that generate two water molecules (the four electron pathway).
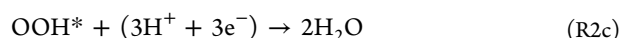
activity contribution from the N-doped sites located on the basal plane into consideration (otherwise, we would have to ascribe all the observed activity to the limited number of Me-N$_x$ sites and/or to the N-doped carbons at the edge of the graphene). Followed spectroscopic and poisoning studies of bNGr reveal that the surface-exposed metallic phases are mostly removed after acid treatment and the residual metals are located in the middle of graphene layers of bNGr. Hence, in our case, the metallic phases cannot directly participate in the ORR, even though they play an important role in increasing reactivity. Detailed discussion will be found in later sections.

3.2. First Electron Transfer. In their theoretical investigations of the ORR mechanism of graphene based catalysts using DFT, presumably due to their knowledge of the well-known ORR mechanism of Pt, most previous researchers have assumed that O_2 adsorption process is the initial step of ORR. This assumption has biased many theoretical studies, causing researchers to focus on identifying good O_2 binding sites on the graphene surface in order to characterize the catalytic active sites.[30] However, our DFT calculations (considering entropic contribution and solvation effect) have found hardly any thermodynamically suitable sites for O_2 binding near the N-doped carbon sites, except for the graphitic-N sites specifically positioned at the edge of the graphene (N_{gra}@edge), as summarized in Figure S3. Thus, if one assumes that the O_2 adsorption process is the essential step for ORR, N_{gra}@edge becomes the only available active site for the N-doped carbon catalyzing process.

However, as discussed above, it is problematic to ascribe all the observed ORR activity merely to the Me-N$_x$ and/or edge graphitic N-doped sites; therefore, we need to consider a catalytic process that does not involve O_2 adsorption. We devised more detailed elementary steps for the first ET using two possibilities: a process of short-range ET to adsorbed O_2 in the inner Helmholtz plane, namely, the ET-IHP mechanism,

$$O_2(aq) \rightarrow O_2^* \qquad (R1a)$$

$$O_2^* + (H^+ + e^-) \rightarrow OOH^* \qquad (R1b)$$

$$OOH^* + (3H^+ + 3e^-) \rightarrow 2H_2O \qquad (R1c)$$

and a process of long-range ET to nonadsorbed O_2 in the outer Helmholtz plane, namely, the ET-OHP mechanism (Scheme 2),

$$O_2(aq) + (H^+ + e^-) \rightarrow ●OOH(aq) \qquad (R2a)$$

$$●OOH(aq) \rightarrow OOH^* \qquad (R2b)$$

$$OOH^* + (3H^+ + 3e^-) \rightarrow 2H_2O \qquad (R2c)$$

where the asterisk denotes the chemical species adsorbed on the surface catalyst. We note that the ET-IHP mechanism requires O_2 adsorption and is analogous to the associative mechanism of ORR on a Pt surface (Figure S4).[31]

The major distinction in both mechanisms is the manner of ET. In the ET-IHP mechanism, direct orbital−orbital overlap provides a channel for ET, and thus the nature of the chemical bond between the electrode surface and O_2 plays a pivotal role in the electrocatalytic processes. In the ET-OHP mechanism, based on the classical double-layer theory,[32] long-range electrolyte−electrode electrostatic interaction governs the electrocatalytic reactions (Figure S5).

Considering the double-layer structure, hydrated cations are present in the OHP and modulate the noncovalent interactions; thus, examining the effect of the ion concentration on the catalytic activity can provide us a clue about the dominance of the "outer-sphere" pathway.[33]

K^+-interference experiments show that high cationic concentration significantly degrades the ORR kinetics of the bNGr catalyst, while only the diffusion current is diminished in the case of Pt (Figure 5b). This trend implies that the contribution of the long-range ET-OHP process is much more significant in our graphene catalysts than it is in Pt catalysts. To ensure that the observed changes in catalytic activities are solely due to variations of cationic concentrations in the OHP,
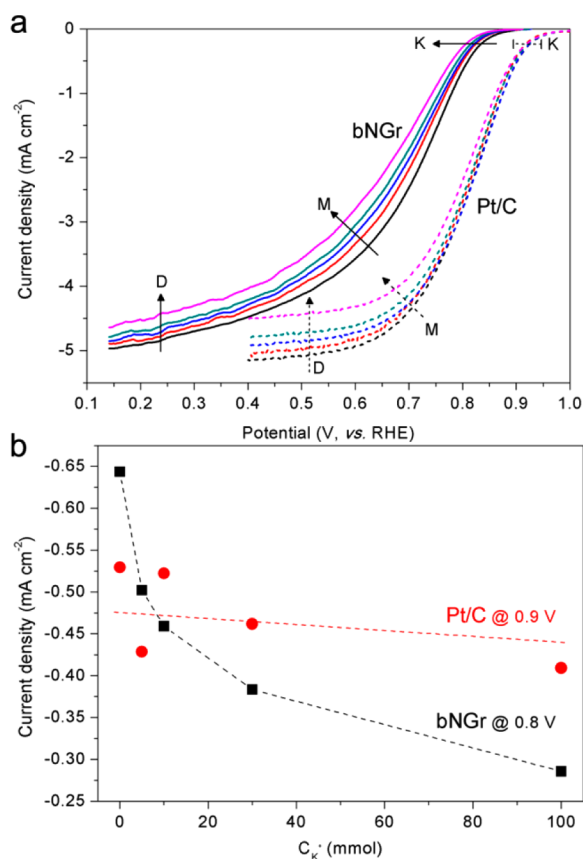
Figure 5. (a) Oxygen reduction polarization curves determined in O_2-bubbled 0.1 M $HClO_4$ with various concentrations of KNO_3 for bNGr and Pt/C (K: kinetic region, M: mixed kinetic-diffusion region, and D: diffusion region). The concentration of KNO_3 was varied from 0 to 5, 10, 30, and 100 mM and is indicated by arrows in the figures. (b) Changes of the kinetic current density (K region in (a) in terms of the additional KNO_3 concentration, obtained at 0.8 and 0.9 V vs RHE for bNGr and Pt/C, respectively.

without including any specific adsorption, we compared the ORR kinetics of the bNGr catalyst for various types of salts with the same concentrations; the kinetics were found to nearly independent of the type of salt (KCN, KCl, KNO_3, and $KClO_4$; Figure S6).

3.3. The Role of N-Doped Sites. If the elementary reaction R2b did not occur fast enough, the reduced oxygen species (●OOH) would stay in OHP and capture another electron and proton to yield H_2O_2 ($2e^-$ pathway), which is inconsistent with the results of our RRDE experiment. Our DFT calculations show that the N-doped sites provide strong adsorption sites for ●OOH (ΔG_{ads}(aq), adsorption free energy in the solvation state for graphitic-N @ basal: −3.20, @ edge: −19.62; pyridinic-N @ basal: −7.94, @ edge: −20.33 kcal mol^{-1}), whereas pristine graphene carbon does not (Figure S7). Therefore, N-doped sites (both at edge and basal sites) act as strong attractors for ●OOH, leading to an immediate binding of ●OOH, followed by stable consecutive reduction steps R1c and R2c, for an overall $4e^-$ pathway.[34]

3.4. Key Factor for Improving Catalytic Activity of ET-OHP. In the ET-OHP mechanism, the location of the electrode potential is the key factor determining the ET kinetics, and therefore the ORR kinetics. Hence, the elevation of the electrode potential is important to enhance the ET rate. By analyzing the differential capacitance, we were able to measure

the potential at the point of zero charge (E_{PZC}), as shown in Figure 6; we found that the ball-milling process elevates the
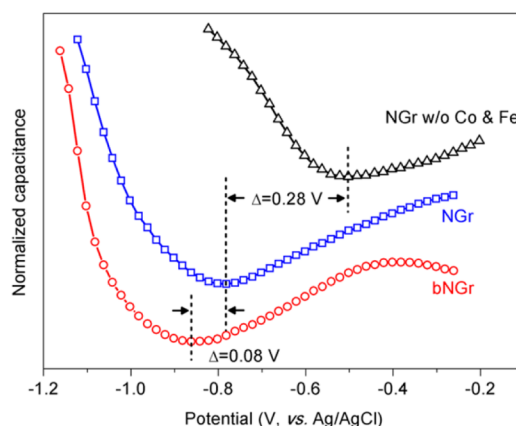

Figure 6. Potential of zero charges, examined in 2 mM of NaF electrolyte with a 100 mHz frequency and a 10 mV potential amplitude.

electrode potential by 0.08 V ($E_{PZC} = -0.78$ V for NGr vs $E_{PZC} = -0.86$ V for bNGr, vs Ag/AgCl). We found that the ball-milling degrades the electrode−catalyst−electrolyte interfaces, increasing the resistance as shown in the impedance measurements (Figure S8). This implies that the catalytic enhancement of the ball-milling process is substantially large enough to compensate the sacrifice in the contact resistance, which can be ascribed by the exponential dependency of the catalytic activity on the electrode potential.

Our DFT results add more insight into the microscopic origin of the elevated electrode potential after ball-milling. We find that the reduction of the lateral length dimension of few-layer graphene modulates the Fermi level (E_F) of the graphene upward (Figure S9); also, a thinner few-layer graphene has a higher E_F.[35] Indeed, the work functions, independently measured using UPS (Figure S10a), were 4.39 eV for NGr and 4.05 eV for bNGr, clearly indicating that E_F is elevated after the ball-milling process, increasing the electrode potential. Similarly, we further postulate that graphitic-N sites are more effective in facilitating ET kinetics because, among the various doping types, graphitic-N doping increases E_F most effectively.[36] However, in terms of stabilizing ●OOH in order to yield an overall four electron pathway, both pyridinic and graphitic sites have their own levels of importance (*vide supra*).

It is further stressed that additional analyses (e.g., EA-ICP, XPS, and Raman spectroscopy, Table S1 and Figure S11) have confirmed that the composition, defect concentration, and types of N-doping of NGr remain almost the same as those of bNGr and hence that the change of electrode potential after the ball-milling process is primarily responsible for the enhanced ORR. The overall energy diagram is provided in Figure 7.

3.5. Role of Metals. Due to the limitations of the detection levels, we cannot completely exclude the possibility of Me-N_x active site formation. However, SWV measurements show an absence of the $Fe^{2+/3+}$ redox couple; XPS measurements also show no peak for metal species (Figure S12a,b), indicating little presence of metal species at the surface after the acid-leaching step. More directly, CN^-, CO, and H_2S poisoning experiments demonstrate insignificant loss of ORR activity of the bNGr catalyst (Figure S12c−e).[57]Fe Mössbauer spectroscopy results support the presence of metallic Fe and Fe−C coordination
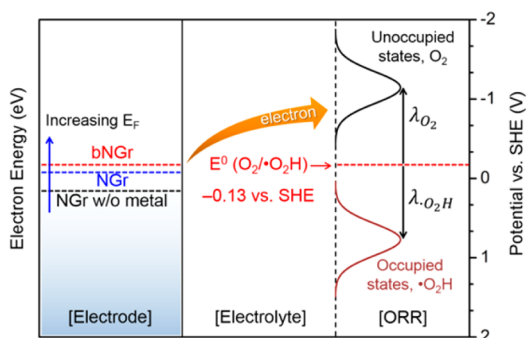
Figure 7. Schematic energy diagram of ET-OHP process from electrode to solvated O_2 molecules. Increased electrode potential (0.08 V, as can be seen in Figure 6) due to the reduction of the graphene dimensions facilitates the rate of ET. Also, the energy of unoccupied states of O_2 is deviated from the equilibrium potential (E^0) due to the solvation effect, which is strongly related with λ (solvent reorganization energy).

rather than $Fe-N_x$ coordination in bNGr,[37,38] that are known to be inactive in acid media (Figure S12f).

Combining all the experimental observations, it is reasonable to conclude that most of the metallic species are buried between the stacked graphene layers, in region inaccessible to O_2. By interacting with the graphene layers, metallic elements can transfer electrons to the graphene layer, and can increase the value of E_F and the ORR activity. From our DFT calculations, we were able to determine that the addition of metallic Fe or Co atoms to various graphene surface models upwardly modulated the value of E_F by transferring electrons from metals to graphene; using such a process, the overall E_F of an electrode can be efficiently increased (Figure S10b). Experimentally, the E_{PZC} of NGr synthesized with no metallic precursors was measured and found to be -0.50 V (vs Ag/AgCl); this is in contrast to the E_{PZC} of NGr synthesized with metallic precursors (-0.78 V vs Ag/AgCl), implying that the presence of metal impurities elevates the electrode potential by 0.28 V. The same increasing tendency of E_F has been observed in independent UPS measurements (Figure S10a). We note that similar explanations of the role of metals have been suggested previously in a model catalyst of a single-walled carbon nanotube system (Fe_4@SWNT).[39] Thus, we conclude that the role of metals in our bNGr catalyst is to increase the electrode potential as located within the interlayer regime (developing Fe-C coordination consistent with [57]Fe Mössbauer spectroscopy results); the presence of metallic elements is essential to enhance the first ET to O_2 for carbon-based catalysts, even though the metals do not act as active sites. Modulation of ORR activity without exposing the metals to the catalyst surface is of practical importance in terms of preserving long-term stability with strong endurance against poisoning effects.

3.6. Single Cell Operations and Long-Term Stability. We have demonstrated the practicability of the bNGr catalyst for single cell PEMFC operation. The polarization curve (IR-free) shown in Figure S13a indicates a 0.91 V open circuit voltage. The mass and volume activities, calculated at 0.8 V, are 3.9 A g^{-1} and 1.7 A cm^{-3}, respectively; these values are comparable to those of catalysts having an $Fe-N_x$ complex as an active site.[40] More importantly, we confirmed the very stable operation of the cell over 1100 h at 0.4 V (Figure S13b), representing a remarkable durability of this catalyst compared

with that of other carbon-based catalysts, even though this catalyst was operated under a more corrosive environment of O_2 (not air).[41] It should be emphasized that this is the first demonstration of single cell operation of PEMFCs with highly stable graphene-based catalysts of enhanced activity without any optimization.

4. CONCLUSION

In summary, we have demonstrated that oxygen adsorption is not necessarily required for the ORR of N-doped graphene and that the initial ET occurs mainly into O_2 molecules in the outer Helmholtz plane, which are contrary to popular belief. The ET-OHP mechanism may resolve the conundrum of finding thermodynamically unstable O_2 binding sites; it allows the participation of basal graphene N-doped sites for the activation of oxygen. This further provides a design principle for graphene based catalysts that will allow us to amplify their activity, increasing the electrode potential. Experimentally, it was shown that the size reduction of few-layer graphene and the inclusion of metallic precursors effectively elevate the electrode potential, resulting in enhancement of the ORR activity. We also demonstrated our nanosized graphene catalysts in single cell operation of PEMFCs with extremely high stability; this insight is expected to supply a guideline to eventually yield a successful replacement of noble-metal based catalysts in the future.

■ ASSOCIATED CONTENT

ⓈSupporting Information

Compositions of the materials for EA and ICP; additional TEM images; EIS/XPS/Raman spectroscopy/SWV/poisoning tests/Mössbauer spectroscopy/UPS results; single cell operations; additional DFT calculation results. This material is available free of charge via the Internet at http://pubs.acs.org.

■ AUTHOR INFORMATION

Corresponding Authors
linus16@kaist.ac.kr
siwoo@kaist.ac.kr

Author Contributions
[§]These authors contributed equally to this work.

Notes
The authors declare no competing financial interest.

■ REFERENCES

(1) Wang, Y.; Chen, K. S.; Mishler, J.; Cho, S. C.; Adroher, X. C. *Appl. Energy* **2011**, *88*, 981.
(2) Chen, Z.; Higgins, D.; Yu, A.; Zhang, L.; Zhang, J. *Energy Environ. Sci.* **2011**, *4*, 3167.
(3) Jasinski, R. *Nature* **1964**, *201*, 1212.

9076

dx.doi.org/10.1021/ja5033474 | *J. Am. Chem. Soc.* 2014, 136, 9070−9077

(4) Gupta, S.; Tryk, D.; Bae, I.; Aldred, W.; Yeager, E. *J. Appl. Electrochem.* **1989**, *19*, 19.

(5) Liu, G.; Li, X. G.; Ganesan, P.; Popov, B. N. *Electrochim. Acta* **2010**, *55*, 2853.

(6) Von Deak, D.; Singh, D.; Biddinger, E. J.; King, J. C.; Bayram, B.; Miller, J. T.; Ozkan, U. S. *J. Catal.* **2012**, *285*, 145.

(7) Oh, H. S.; Kim, H. *J. Power Sources* **2012**, *212*, 220.

(8) Ferrandon, M.; Kropf, A. J.; Myers, D. J.; Artyushkova, K.; Kramm, U.; Bogdanoff, P.; Wu, G.; Johnston, C. M.; Zelenay, P. *J. Phys. Chem. C* **2012**, *116*, 16001.

(9) Li, Y.; Zhou, W.; Wang, H.; Xie, L.; Liang, Y.; Wei, F.; Idrobo, J. C.; Pennycook, S. J.; Dai, H. *Nat. Nanotechnol.* **2012**, *7*, 394.

(10) Lefevre, M.; Proietti, E.; Jaouen, F.; Dodelet, J. P. *Science* **2009**, *324*, 71.

(11) Wu, G.; More, K. L.; Johnston, C. M.; Zelenay, P. *Science* **2011**, *332*, 443.

(12) Rao, C. V.; Cabrera, C. R.; Ishikawa, Y. *J. Phys. Chem. Lett.* **2010**, *1*, 2622.

(13) Subramanian, N. P.; Li, X.; Nallathambi, V.; Kumaraguru, S. P.; Colon-Mercado, H.; Wu, G.; Lee, J.-W.; Popov, B. N. *J. Power Sources* **2009**, *188*, 38.

(14) Oh, H.-S.; Oh, J.-G.; Roh, B.; Hwang, I.; Kim, H. *Electrochem. Commun.* **2011**, *13*, 879.

(15) Kiuchi, H.; Niwa, H.; Kobayashi, M.; Harada, Y.; Oshima, M.; Chokai, M.; Nabae, Y.; Kuroki, S.; Kakimoto, M.-a.; Ikeda, T.; Terakura, K.; Miyata, S. *Electrochim. Acta* **2012**, *82*, 291.

(16) Maldonado, S.; Stevenson, K. J. *J. Phys. Chem. B* **2005**, *109*, 4707.

(17) Luo, Z. Q.; Lim, S. H.; Tian, Z. Q.; Shang, J. Z.; Lai, L. F.; MacDonald, B.; Fu, C.; Shen, Z. X.; Yu, T.; Lin, J. Y. *J. Mater. Chem.* **2011**, *21*, 8038.

(18) Niwa, H.; Horiba, K.; Harada, Y.; Oshima, M.; Ikeda, T.; Terakura, K.; Ozaki, J.; Miyata, S. *J. Power Sources* **2009**, *187*, 93.

(19) Lai, L. F.; Potts, J. R.; Zhan, D.; Wang, L.; Poh, C. K.; Tang, C. H.; Gong, H.; Shen, Z. X.; Jianyi, L. Y.; Ruoff, R. S. *Energy Environ. Sci.* **2012**, *5*, 7936.

(20) Kim, H.; Lee, K.; Woo, S. I.; Jung, Y. *Phys. Chem. Chem. Phys.* **2011**, *13*, 17505.

(21) Perdew, J. P.; Burke, K.; Ernzerhof, M. *Phys. Rev. Lett.* **1996**, *77*, 3865.

(22) Harihara, P. C.; Pople, J. A. *Chem. Phys. Lett.* **1972**, *16*, 217.

(23) Kresse, G.; Furthmuller, J. *Comput. Mater. Sci.* **1996**, *6*, 15.

(24) Fishman, M.; Zhuang, H. L. L.; Mathew, K.; Dirschka, W.; Hennig, R. G. *Phys. Rev. B* **2013**, *87*, 245402.

(25) Wang, L.; He, X. *J. Nanotechnol. Eng. Med.* **2010**, *1*, 041004.

(26) Jeon, I. Y.; Choi, H. J.; Jung, S. M.; Seo, J. M.; Kim, M. J.; Dai, L. M.; Baek, J. B. *J. Am. Chem. Soc.* **2013**, *135*, 1386.

(27) Janik, M. J.; Taylor, C. D.; Neurock, M. *J. Electrochem. Soc.* **2009**, *156*, B126.

(28) Gojković, S. L.; Gupta, S.; Savinell, R. F. *J. Electroanal. Chem.* **1999**, *462*, 63.

(29) Peuckert, M.; Yoneda, T.; Betta, R. A. D.; Boudart, M. *J. Electrochem. Soc.* **1986**, *133*, 944.

(30) Yu, L.; Pan, X.; Cao, X.; Hu, P.; Bao, X. *J. Catal.* **2011**, *282*, 183.

(31) Nørskov, J. K.; Rossmeisl, J.; Logadottir, A.; Lindqvist, L.; Kitchin, J. R.; Bligaard, T.; Jónsson, H. *J. Phys. Chem. B* **2004**, *108*, 17886.

(32) Bard, A. J.; Faulkner, L. R. *Electrochemical Methods: Fundamentals and Applications*; Wiley: New York, 2000.

(33) Strmcnik, D.; Kodama, K.; van der Vliet, D.; Greeley, J.; Stamenkovic, V. R.; Markovic, N. M. *Nat. Chem.* **2009**, *1*, 466.

(34) Zhang, L.; Xia, Z. *J. Phys. Chem. C* **2011**, *115*, 11170.

(35) Guinea, F. *Phys. Rev. B* **2007**, *75*, 235433.

(36) Schiros, T.; Nordlund, D.; Pálová, L.; Prezzi, D.; Zhao, L.; Kim, K. S.; Wurstbauer, U.; Gutiérrez, C.; Delongchamp, D.; Jaye, C.; Fischer, D.; Ogasawara, H.; Pettersson, L. G. M.; Reichman, D. R.; Kim, P.; Hybertsen, M. S.; Pasupathy, A. N. *Nano Lett.* **2012**, *12*, 4025.

(37) Kramm, U. I.; Herranz, J.; Larouche, N.; Arruda, T. M.; Lefevre, M.; Jaouen, F.; Bogdanoff, P.; Fiechter, S.; Abs-Wurmbach, I.; Mukerjee, S.; Dodelet, J.-P. *Phys. Chem. Chem. Phys.* **2012**, *14*, 11673.

(38) Zhang, S.; Zhang, H.; Liu, Q.; Chen, S. *J. Mater. Chem. A* **2013**, *1*, 3302.

(39) Deng, D.; Yu, L.; Chen, X.; Wang, G.; Jin, L.; Pan, X.; Deng, J.; Sun, G.; Bao, X. *Angew. Chem., Int. Ed.* **2013**, *52*, 371.

(40) Jaouen, F.; Proietti, E.; Lefevre, M.; Chenitz, R.; Dodelet, J.-P.; Wu, G.; Chung, H. T.; Johnston, C. M.; Zelenay, P. *Energy Environ. Sci.* **2011**, *4*, 114.

(41) Peng, H. L.; Mo, Z. Y.; Liao, S. J.; Liang, H. G.; Yang, L. J.; Luo, F.; Song, H. Y.; Zhong, Y. L.; Zhang, B. Q. *Sci. Rep.* **2013**, *3*, 1765.

9077

dx.doi.org/10.1021/ja5033474 | *J. Am. Chem. Soc.* 2014, 136, 9070–9077